PERGAMON

International Journal of Heat and Mass Transfer 45 (2002) 5133–5141

International Journal of HEAT and MASS TRANSFER

www.elsevier.com/locate/ijhmt

Numerical computation of fluid flow and heat transfer in microchannels

K.C. Toh, X.Y. Chen, J.C. Chai *

School of Mechanical and Production Engineering, Nanyang Technological University, Nanyang Avenue, Singapore 639798, Singapore

Received 14 January 2002; received in revised form 14 June 2002

Abstract

Three-dimensional fluid flow and heat transfer phenomena inside heated microchannels is investigated. The steady, laminar flow and heat transfer equations are solved using a finite-volume method. The numerical procedure is validated by comparing the predicted local thermal resistances with available experimental data. The friction factor is also predicted in this study. It was found that the heat input lowers the frictional losses, particularly at lower Reynolds numbers. At lower Reynolds numbers the temperature of the water increases, leading to a decrease in the viscosity and hence smaller frictional losses.

Keywords: Fluid flow and heat transfer; Microchannels

1. Introduction

With the development of new high performance chips, the ability to remove heat from the high heat flux region around the chips becomes an important factor in the design of reliable computing systems. Since the availability of microfabrication techniques, these devices have also been made more compact, leading to even higher heat fluxes. In the coming years, it is projected that these heat fluxes may exceed 100 W/cm^2 [1]. Air-cooling techniques are unlikely to be able to meet the cooling needs of these high heat flux electronic packages. As a result, there is increased interest in microchannel liquid cooling techniques [2–13].

Adams et al. [2] conducted single-phase flow studies in microchannels using water as the working fluid. Two diameters of the circular microchannels, namely 0.76 and 1.09 mm, were used in the investigation. It was found that the Nusselt numbers are larger than those encountered in macrochannels.

Peng and Peterson [3] investigated water flows in rectangular microchannels with hydraulic diameters ranging from 0.133 to 0.367 mm. In laminar flows, it was found that the heat transfer depends on the aspect ratio and the ratio of the hydraulic diameter to the center-to-center distance of the microchannels.

Qu et al. [4,5] investigated flow and heat transfer in trapezoidal silicon microchannels. The measured friction factors were found to be higher than the numerical predictions conducted by the authors. The difference was attributed to the wall "roughness". A roughness–viscosity model was proposed to explain the experimental observations. It was also found that the numerically predicted Nusselt numbers are smaller than the experimentally determined Nusselt numbers. The concept used to propose the roughness–viscosity model for friction factors was used in the heat transfer study to obtain better comparisons with experimental data.

Fedorov and Viskanta [6] reported numerical results based on the experiments of Kawano et al. [7]. The friction factor and thermal resistance were well predicted by the authors. A finite-volume method (FVM) was used to solve the three-dimensional Navier–Stokes equations and the energy equation. It was noticed that the overall *fRe* varies (almost linearly) with the Reynolds number.

* Corresponding author. Tel.: +65-6790-4270; fax: +65-6792-4062.

E-mail address: mckchai@ntu.edu.sg (J.C. Chai).

0017-9310/02/$ - see front matter © 2002 Published by Elsevier Science Ltd.
PII: S0017-9310(02)00223-5

Nomenclature

A	flow area
C_p	specific heat
D_h	hydraulic diameter
f	friction factor
H_c	channel height
H_t	total height
k	thermal conductivity
L_h	heater length
L_t	total length
P	wetted perimeter
p	pressure
q	heat flux
$\dot{Q}$	total volumetric flow rate
R	thermal resistance
Re	Reynolds number
T	temperature
T_{in}	inlet temperature
T_{max}	maximum temperature
u	velocity
u_{ave}	average channel velocity
W_c	channel width
W_h	heater width
W_s	substrate width
W_t	specific heat
x, y, z	coordinate directions

Greek symbols

μ	viscosity
ρ	density

Subscripts

ave	average
c	channel
s	substrate
t	total

The thermal resistance decreases with Reynolds number and reaches an asymptote at high Reynolds numbers.

Lim et al. [8] conducted experimental study on water flows in microtubes. The diameters range from 49.3 to 701.9 μm. It was found that when the microtubes diameters are below 300 μm, the fRe decreases (departs from the fully developed fRe of 64) as the diameter decreases. For example, when the diameter is 49.3 μm, the fRe is 55.6. An analytical study [9] was conducted to explain the experimentally observed trend. The authors attributed the decrease in fRe to the reduction in the viscosity of water due to viscous dissipation in microtubes with diameters smaller than 300 μm.

Samalam [10] reported results of a theoretical study based on the experimental setup of Tuckerman [11]. A thermal resistance correlation was developed by Samalam [10]. Weisberg et al. [12] reported numerical results for Tuckerman's experiments. The flow inside the microchannels is assumed to be hydrodynamically and thermally fully developed. Reasonable agreements with the experimental results were reported. Due to the fully developed flow and heat transfer assumptions, detailed comparisons of the local thermal resistance with the experimental results were not carried out. Comparisons with Samalam's correlation showed that the numerical predictions matched the correlation reported by Samalam [10] very well for a set of parameters. Ng et al. [13] reported results for a configuration which is geometrically similar to Tuckerman's experiment but with larger dimensions. As a result, no comparisons with the experimental data were reported. To the best knowledge of the present authors, there is no published work on the numerical computations of Tuckerman's experimental setup which accounts for the hydrodynamic and thermal developments of the flow.

In this article, a detailed numerical study is conducted on the experimental conditions of Tuckerman [11]. Both the flow and energy fields are allowed to develop in the present study. The FVM of Patankar [14] is used to model the conjugate heat transfer through the heat sink and the flow and heat transfer development region inside the microchannels. The numerically obtained local thermal resistances are compared with available experimental measurements. The effects of the liquid mass flowrate in the microchannels, heat flux through the heat sink and size of the microchannel heat sinks are also examined. The objectives of the article are to (1) access the capability and accuracy of the FVM for prediction of flow and heat transfer characteristics in microchannel liquid cooling systems and (2) gain understanding of the various effects encountered in the flow through the microchannel.

The remainder of this article is divided into three sections. The physical situation considered and the computational domain used to simulate the experimental setup is presented in the next section. This is followed by a section describing the mathematical formulation of the problem. The numerical method used to solve the governing equations is discussed briefly in this section. The results obtained numerically are compared with the experimental data of Tuckerman [11]. The effects of various parameters on the thermal resistance are also discussed in this section. Finally, some remarks are given to conclude the article.

2. The physical model and the computational domain

Fig. 1 shows the schematic drawing of the test configuration. Heat, supplied to the silicon substrate through a 1 cm × 1 cm heating area, is removed by flowing water through a number of microchannels. The width and height of the microchannels are W_c and H_c respectively. The thickness of the silicon substrate is $H_t - H_c$. The total length of the microchannels is L_t. The heating area is located at the entrance of the microchannels and is centered across the width of the whole microchannel heat sink as shown in Fig. 1b. A uniform heat flux of q is provided to heat the microchannels. The inlet temperature of the cooling water is 20 °C. The dimensions for four different sets of microchannels are given in Table 1. Using these dimensions, there will be 150 microchannels in Case 1 and 200 microchannels in each of the Cases 2, 3, and 4. It should be mentioned that Case 0 is the same as Case 1 but with a smaller flowrate.

Table 1
Parameters for four different sets of microchannels

	Case				
	0	1	2	3	4
L_t (cm)	2	2	1.4	1.4	1.4
W_t (cm)	1.5	1.5	2	2	2
W_c (μm)	64	64	56	55	50
W_s (μm)	36	36	44	45	50
H_t (μm)	489	489	533	430	458
H_c (μm)	280	280	320	287	302
$\dot{Q}^a$ (cm³/s)	1.277	1.86	4.7	6.5	8.6
q (W/cm²)	34.6	34.6	181	277	790
Number of channels	150	150	200	200	200

[a] Total flow rate through the heat sink assembly.

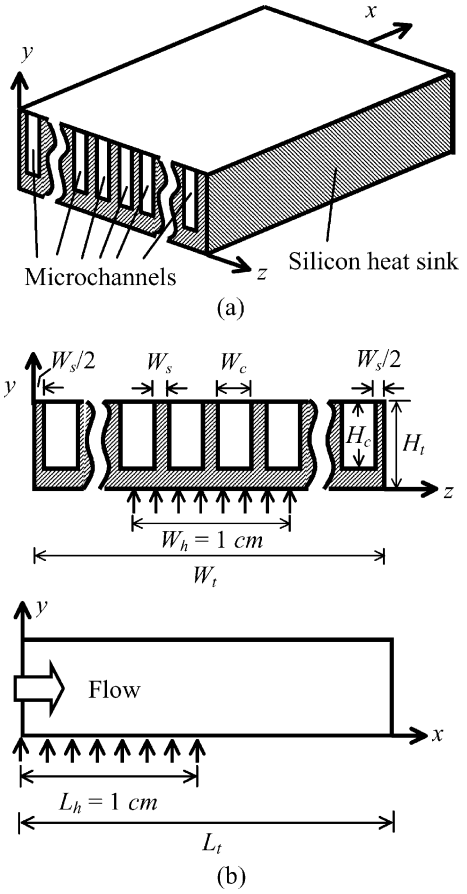

Fig. 1. (a) Schematic of the microchannels, (b) dimensions of the microchannels.

It is computationally intensive to model the whole microchannel heat sink with either 150 or 200 microchannels. As a result, a simplified computational domain is used in this study. Fig. 2 shows this computational domain. Care must be taken in the modeling of the heat flux. If a computational module towards the outer edges of the heat sink is chosen, the actual heat input can be zero or smaller than the uniform heat input supplied by the heater. As a result, a microchannel module at the center of the heat sink is chosen for our study. At this location, the heat flux is the same as that quoted in the experiment. This is because there is very little spreading of the heat towards the sides at the center of the heat

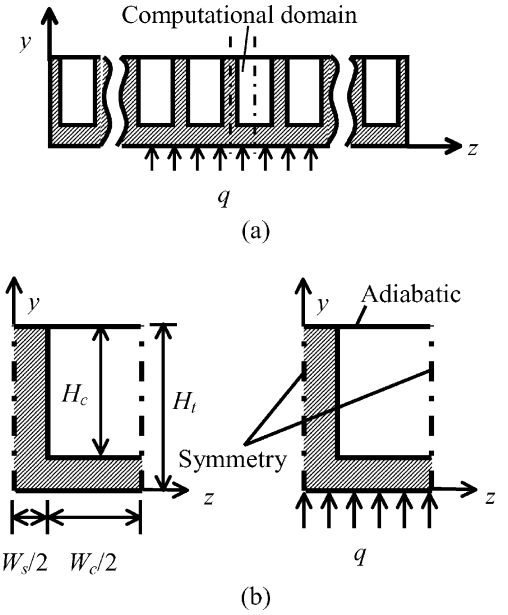

Fig. 2. Computational domain: (a) normal view, (b) enlarged view.

sink. It is clear that the heat sink exhibits geometrical symmetries. Due to the heat sink module chosen in this study, planes of symmetry can also be identified for the heat transfer part of the problem. With the above simplifications, only half of the fin and half of the microchannel are modeled as shown in Fig. 2b. The left ($z = 0$) boundary and the right ($z = W_s/2 + W_c/2$) boundary are planes of symmetry. At the bottom wall ($y = 0$), the given fluxes of q and 0 are imposed over the heated area and the trailing edge of the heat sink, respectively. In the experiment, the top wall is exposed to an ambient environment. However, no information about the convective heat transfer coefficient is available. Since the top wall ($y = H_t$) is made of glass and its conductivity is two orders of magnitude lower than that of silicon, it is assumed to be an adiabatic wall. The front boundary ($x = 0$) and back boundary ($x = L_t$) are the inlet and outlet boundaries respectively.

3. Mathematical formulation

The mathematical formulation of the problem is described in this section. The numerical method used for this study is also discussed here.

3.1. Governing equations

In this article, the flow and heat transfer is assumed to be steady, incompressible and laminar. Some of the properties are allowed to vary with temperature and is discussed in a later section. The continuity, momentum and energy equations for the problem can be written in Cartesian tensor notation as

Continuity

$$\frac{\partial(\rho u_j)}{\partial x_j} = 0 \tag{1}$$

Momentum

$$\frac{\partial(\rho u_j u_i)}{\partial x_j} = \frac{\partial}{\partial x_j}\left(\mu\frac{\partial u_i}{\partial x_j}\right) + \frac{\partial}{\partial x_j}\left(\mu\frac{\partial u_j}{\partial x_i}\right) - \frac{2}{3}\frac{\partial}{\partial x_i}\left(\mu\frac{\partial u_k}{\partial x_k}\right) - \frac{\partial p}{\partial x_i} \tag{2}$$

Energy

$$\frac{\partial(\rho C_p u_j T)}{\partial x_j} = \frac{\partial}{\partial x_j}\left(k\frac{\partial T}{\partial x_j}\right) + \mu\dot{\gamma}^2 \tag{3a}$$

$$|\dot{\gamma}| = \sqrt{2\left[\left(\frac{\partial u}{\partial x}\right)^2 + \left(\frac{\partial v}{\partial y}\right)^2 + \left(\frac{\partial w}{\partial z}\right)^2\right] + \left(\frac{\partial u}{\partial y} + \frac{\partial v}{\partial x}\right)^2 + \left(\frac{\partial u}{\partial z} + \frac{\partial w}{\partial x}\right)^2 + \left(\frac{\partial v}{\partial z} + \frac{\partial w}{\partial y}\right)^2} \tag{3b}$$

3.2. Boundary conditions

Boundary conditions for the six boundaries are specified for this simplified computational domain. At the entrance of the heat sink assembly ($x = 0$), two types of boundaries are encountered. Water flows through the microchannels and removes heat conducted to the surface of the heat sink. The remainder of the entrance is occupied by the silicon substrate. At the microchannels sections, the inlet water (axial) velocity and the inlet water temperature are specified. In calculating the inlet velocity, the water is assumed to be evenly distributed into all microchannels. The transverse velocities at the inlet are assumed to be zero. On the silicon substrate, the velocities are zero, and it is assumed to be an adiabatic surface. At the exit ($x = L_t$), zero gradient conditions are imposed on the transverse velocities and the temperature. The axial velocity is calculated to ensure mass conservation over the whole solution domain. Symmetry is imposed on the left ($z = 0$) and right ($z = W_c + W_s$) boundaries. At the bottom boundary, the velocities are zero (silicon substrate). For $x \leqslant L_h$, a constant heat flux of q is imposed at the bottom wall. The remainder of the bottom wall ($x > L_h$) is assumed to be adiabatic. The top wall ($y = H_t$) is assumed to be adiabatic and has zero velocities.

3.3. Properties of water and silicon substrate

As mentioned earlier, some properties of water are allowed to vary with temperature. The functional relations between density, specific heat, thermal conductivity and viscosity with temperature are [15]

$$\rho = \frac{a_0 + a_1 T + a_2 T^2 + a_3 T^3 + a_4 T^4 + a_5 T^5}{1 + a_6 T} \tag{4}$$

$$C_p = b_0 + b_1 T + b_2 T^2 + b_3 T^3 \tag{5}$$

$$k = c_0 + c_1 T + c_2 T^2 \tag{6}$$

$$\mu = d_0 10^{d_1/(T - d_2)} \tag{7}$$

In Eqs. (4)–(7), thermal conductivity k is in W/m K, viscosity μ is in N s/m^2 and temperature T is in °C respectively. The various constants are listed in Table 2. The thermal conductivity of the silicon is taken as 148 W/m K.

Table 2
Constants in properties vs. temperature correlations

x	a_x	b_x	c_x	d_x
0	999.84	8958.9	−0.58166	2.414×10^{-5}
1	18.225	−40535	6.3556×10^{-3}	247.8
2	-7.92×10^{-3}	0.11243	-7.964×10^{-6}	140.0
3	-5.545×10^{-5}	-1.014×10^{-4}		
4	1.498×10^{-7}			
5	-3.933×10^{-10}			
6	1.816×10^{-2}			

3.4. Numerical method

In this article, the FVM of Patankar [14] is used to solve the continuity, momentum and energy equations. Since a detailed discussion of the FVM is available in Patankar [14], only a very brief description of the major features of the FVM used is given here.

In the FVM, the domain is divided into a number of control volumes such that there is one control volume surrounding each grid point. The grid point is located in the center of a control volume. The governing equation is integrated over each control volume to derive an algebraic equation containing the grid point values of the dependent variable. The discretization equation then expresses the conservation principle for a finite control volume just as the partial differential equation expresses it for an infinitesimal control volume. The resulting solution implied that the integral conservation of quantities such as mass, momentum and energy is exactly satisfied for any control volume and of course, for the whole domain. The power-law scheme is used to model the combined convection-diffusion effect in the transport equations. The SIMPLER algorithm of Patankar [14] is used to resolve the pressure–velocity coupling. The resulting algebraic equations are solved using a line-by-line Tri-Diagonal Matrix Algorithm. In the present study, a solution is deemed converged when the mass imbalance in the continuity equation is less than 10^{-11}.

4. Results and discussions

The results obtained using the FVM are presented in this section. The numerical solutions are first compared with the experimentally measured thermal resistances. Once the model has been validated, the parametric studies are conducted to study the effects of flow rate, heat flux, and heating area on the thermal resistance and friction factor.

To compare with experimental data, the local thermal resistance is calculated using

$$R(x) = \frac{T_{\max}(x) - T_{\text{in}}}{q} \tag{8}$$

In Eq. (8), $R(x)$, $T_{\max}(x)$, T_{in}, and q are the thermal resistance at x cm from the entrance, the maximum temperature at x cm from the entrance, the inlet water temperature and the heat flux at the heating area.

In addition to the thermal resistance, the local and overall *fRe* are also calculated. The friction factor and Reynolds number are calculated using

$$f \equiv \frac{-(\mathrm{d}p/\mathrm{d}x)D_{\text{h}}}{\rho u_{\text{ave}}^2/2} \tag{9}$$

$$Re \equiv \frac{\rho u_{\text{ave}} D_{\text{h}}}{\mu} \tag{10}$$

$$D_{\text{h}} \equiv \frac{4A}{P} = \frac{2H_{\text{c}}W_{\text{c}}}{W_{\text{c}} + H_{\text{c}}} \tag{11}$$

Since most friction factor measurements are conducted using cold flow (zero heat input) condition, the density and viscosity for the friction factor (Eq. (9)) and Reynolds number (Eq. (10)) calculations are evaluated at the inlet temperature which is 20 °C. The local *fRe* is calculated based on the local pressure gradient. The overall *fRe* is calculated based on the pressure difference between the inlet and the outlet.

A grid independence study is carried out using $100 \times 32 \times 16$ and $200 \times 64 \times 32$ control volumes in the x-direction, y-direction and z-direction respectively, based on Case 4 microchannels with the flow rate and heat flux specified in Table 1. When the flowrate is 8.6 cm^3/s, the thermal resistances predicted using these grid sizes are 0.1046 cm^2 K/W and 0.1037 cm^2 K/W respectively. This represents a 0.87% error in the thermal resistance. For the same flowrate, the predicted *fRe* values (with temperature-dependent properties) using the coarse and fine grids are 40.65 and 40.71 respectively. As a result, the results presented in this article are obtained using the coarser grid of $100 \times 32 \times 16$ control volumes.

4.1. Temperature distribution and thermal resistance

The temperature distributions at four y–z cross-sections along the channel are shown in Fig. 3 for Case 0. The four sections ($x = 1$, 3, 6, 9 mm) are all in the heated area. It can be seen that the isotherms in the fluid are closer than that in the solid due to the different thermal conductivities. It also can be seen that the isotherms in the fluid are the closest at the entrance area and then spread out gradually along the channel, that means the heat transfer is the highest at the entrance, and it decreases along the channel.

Tuckerman [11] reported the maximum thermal resistance for the five cases tabulated in Table 1. These thermal resistances were reported at $x = 0.9$ cm. Table 3 shows the comparisons between the thermal resistances measured by Tuckerman and those calculated (using Eq. (8)) in this study. It can be seen that the present calculations predicted the thermal resistances very well. Fig. 4

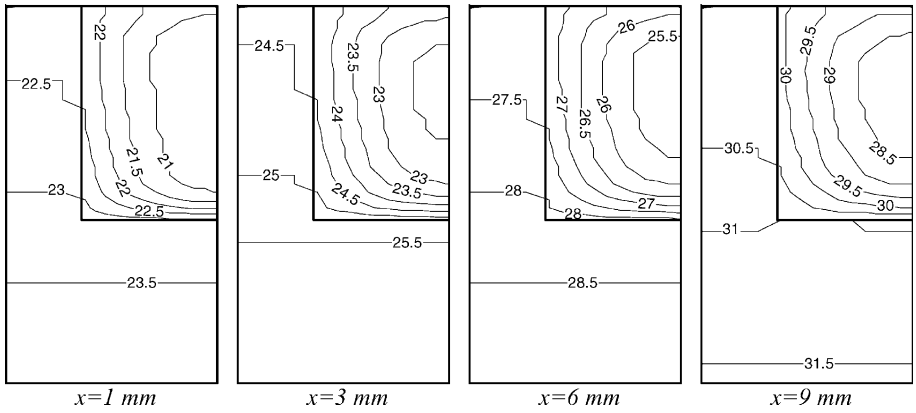

Fig. 3. Temperature distribution at four different cross-sections along the channel.

Table 3
Comparisons of thermal resistances at $x = 0.9$ cm

Case	q (W/cm^2)	$\dot{Q}$ (cm^3/s)	R (cm^2 K/W)	
			Tuckerman's experiment	Present calculation
0	34.6	1.277	0.277	0.331
1	34.6	1.86	0.280	0.253
2	181	4.7	0.110	0.157
3	277	6.5	0.113	0.128
4	790	8.6	0.090	0.105

shows the local thermal resistance obtained in the present study. Comparisons with the experimentally obtained thermal resistance at $x = 0.9$ cm are also shown graphically in Fig. 4. In Case 1, it can be seen that the maximum local thermal resistance occurs around $x = 0.9$ cm. The maximum thermal resistance is lower than the experimentally measured value. This is consistent with the predictions of Weiberg et al. [12] and Samalam [10]. It should also be mentioned that the experimentally measured maximum thermal resistances for Case 1 for flow rates of 1.86 and 1.277 cm^3/s (also called Case 0 in Fig. 4 and Table 3) are 0.28 and 0.277 cm^2 K/W respectively. Physically, as the flow rate decreases the maximum temperature should increase leading to an increase in the thermal resistance. The reversed trend is noticed in the experimental measurements. This is most probably due to experimental uncertainty in the measurements. It can be also seen from Fig. 4 that the thermal resistances increase linearly along the channels except the very short entrance region. That means after the short entrance area, the flow is thermally developed. The local thermal resistance predicted for Case 1 with a smaller volumetric flow rate of 1.277 cm^3/s (called Case 0 in Table 1 and Fig. 4) is compared with the experimental data of Tuckerman [11] in Fig. 5. Once again, it can be seen that the present calculation predicted the local thermal resistance very well. With the exception of Case 1, the computed maximum thermal resistances were higher than the experimentally measured values. This is expected as the top wall is assumed to be adiabatic in the present study. Now that the numerical

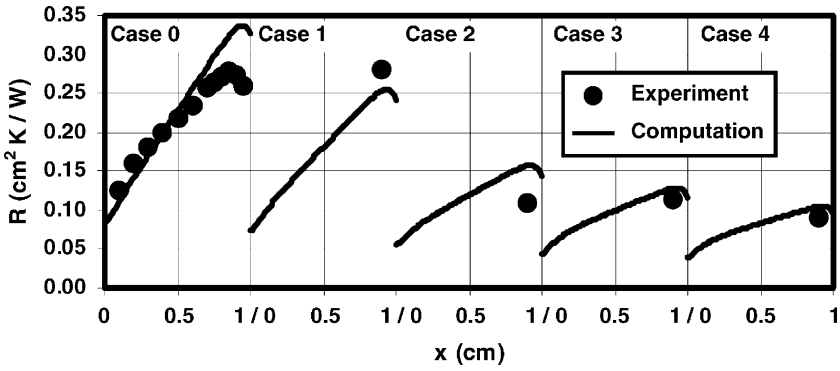

Fig. 4. Local thermal resistances for the five cases listed in Table 1.

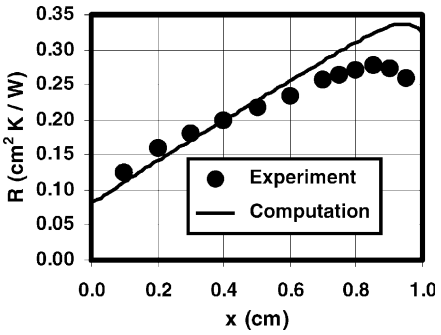

Fig. 5. Comparison of the local thermal resistance between Tuckerman's experiment and the present computation for Case 0 microchannels.

procedure used in this study has been validated with the experimental data of Tuckerman [11], effects of various parameters on the thermal resistance and friction factors are presented.

Fig. 6 shows the thermal resistance at $x = 0.9$ cm as a function of the Reynolds number. It can be seen that the thermal resistance decreases with increasing Reynolds number. This is because as the velocity increases, the maximum temperature of the silicon substrate decreases leading to a smaller thermal resistance.

4.2. Friction factor

The *overall fRe* is shown in Fig. 7 as a function of the Reynolds number for Case 1 microchannels. Two sets of predictions are shown in Fig. 7. These are based on constant water properties (evaluated at the inlet temperature; white circles) and temperature-dependent water properties (black circles). For reference purposes, the fully developed *fRe* for a rectangular channel with an aspect ratio (Case 1) of 4.375 is 73.84.

It can be seen that the *overall fRe* obtained using constant water properties is almost constant for the

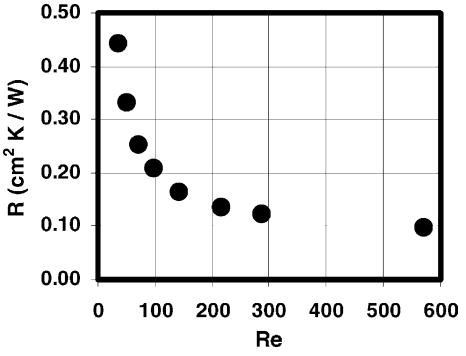

Fig. 6. Effect of Reynolds number on the thermal resistance ($x = 0.9$ cm, Case 1 microchannels).

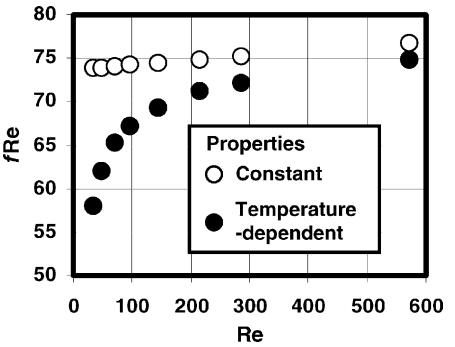

Fig. 7. Effect of temperature on the *fRe* (Case 1).

range of Reynolds number examined. At $Re = 34.6$, the *fRe* predicted using the FVM is 73.8 which for all practical purposes is the theoretical fully developed *fRe* (73.84). As the Reynolds number increases, the *fRe* increases slightly due to the entrance effect. This can be explained using Fig. 8a. Fig. 8a shows the local *fRe* when the water properties are assumed constant. The following can be observed as the Reynolds number increases: (1) the maximum local *fRe* at the entrance increases, (2) the entrance length increases and (3) remote from the inlet ($x \to 2$ cm), the *fRe* reaches the same value which is the theoretical fully developed *fRe* for all Reynolds numbers.

When the properties are allowed to change with temperature, the *fRe* drops drastically at smaller Reynolds numbers. A further investigation shows that as long as the viscosity of the water is evaluated at the inlet temperature and is not allowed to change with the temperature, the *fRe* is the same as that obtained using constant water properties. When the viscosity of the water is allowed to change with the temperature, the *fRe* for temperature-dependent properties shown in Fig. 7 is obtained. This is true no matter if the other properties are allowed to change with temperature or remain constant at the inlet temperature. As a result, it can be concluded that the drastic change in the *fRe* is due to the change in the viscosity of the water. At lower Reynolds numbers, the water attains higher temperatures leading to lower viscosities. This resulted in lower pressure drop and thus the decrease in the values of *fRe*. At higher Reynolds numbers, the water temperatures are almost the same as the inlet temperature at the exit. As a result, the viscosity is almost constant. As expected, the *fRe* approaches the constant properties (constant viscosity) cases as shown in Fig. 7.

Fig. 8b shows the local *fRe* for temperature-dependent viscosity situations. For reference purposes, the 1 cm long heater is located between the inlet ($x = 0$) and $x = 1$ cm. The following can be observed as the Reynolds number increases: (1) the maximum local *fRe* at the entrance increases, (2) remote from ($x \to 2$ cm), the

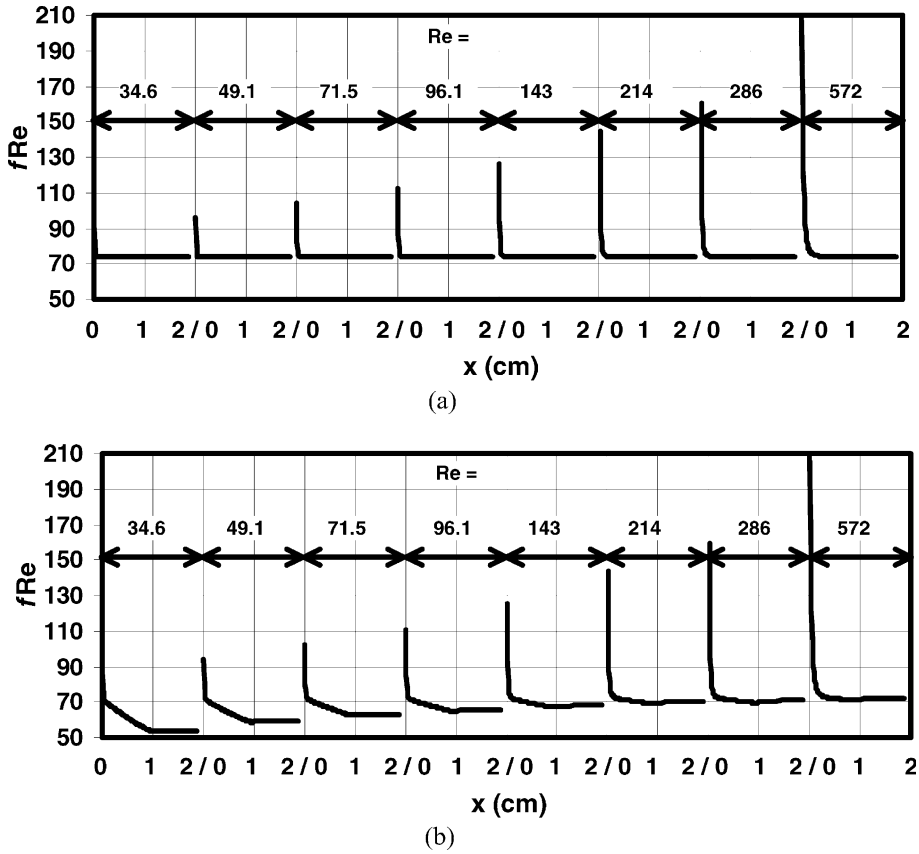

Fig. 8. Effect of Reynolds number on the local *fRe* (Case 1 microchannels). (a) Constant water properties, (b) temperature-dependent water properties.

inlet, the *fRe* decreases as the Reynolds number decreases, (3) the local *fRe* decreases continuously in the heater section ($0 \leqslant x \leqslant 1$ cm), (4) the decrease is larger at smaller Reynolds numbers, and (5) the local *fRe* becomes constant in the unheated section ($x > 1$ cm).

Fig. 9 shows an enlarged view of the local *fRe* plot for $Re = 34.6$. When the water properties are constant, the local *fRe* attained a constant value of 73.8 when $Re = 34.6$ (from the present computation) once the flow is hydrodynamically fully developed. When the water viscosity is allowed to change with the temperature, the local *fRe* continues to decrease in the heater section due to the increase in the water temperatures leading to lower water viscosities.

From these observations, it can be concluded that cold flow conditions can lead to significantly over prediction of the frictional losses. As a result, the effect of the heat input on the properties (particularly the viscosity) should be taken into account when estimating the frictional losses. Lim et al. [8,9] also attributed the decrease in the *fRe* to the decrease in viscosity due to viscous dissipation.

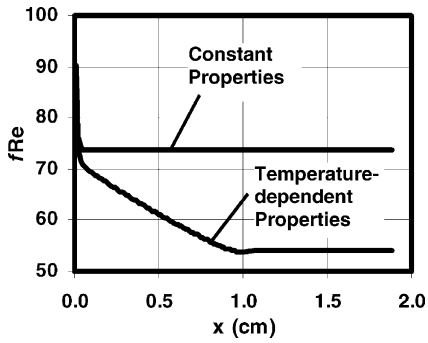

Fig. 9. Comparison of the local *fRe* obtained using constant and temperature dependent water properties for $Re = 34.6$ (Case 1 microchannels).

5. Concluding remarks

The heat transfer inside four microchannels heat sinks has been presented in this article. The predicted thermal resistances compare well with available experi-

mental data. The local thermal resistance is also well predicted for a situation where experimental data is available. The numerical procedure correctly predicted the location of the maximum thermal resistance and the drop (due to axial heat spreading) in the thermal resistance towards the trailing edge of the heater.

The friction factor is reported in the form of the product of the friction factor f and the Reynolds number Re (fRe). The results indicate that the cold flow fRe matches the theoretical fully developed fRe for Case 1 microchannels heat sink. With heating, the fRe decreases drastically at lower Reynolds number. This is because at small Reynolds numbers, the water temperature attains a higher value. This leads to lower water viscosities and thus the drastic drop in the values of fRe. It was also found that the other properties of water namely, density, specific heat and thermal conductivity have insignificant effect on the fRe product for the Case 1 microchannel heat sinks examined in this article.

References

[1] A. Bar-Cohen, Thermal management of microelectronics in the 21st century, Proceedings of the IEEE/CPMT Electronic Packaging Technology Conference (1997) 29–33.

[2] T.M. Adams, S.I. Abdel-Khalik, S.M. Jeter, Z.H. Qureshi, An experimental investigation of single-phase forced convection in microchannels, Int. J. Heat Mass Transfer 41 (1998) 851–857.

[3] X.F. Peng, G.P. Peterson, Convective heat transfer and flow friction for water flow in microchannel structures, Int. J. Heat Mass Transfer 39 (1996) 2599–2608.

[4] W. Qu, G.M. Mala, D. Li, Pressure-driven water flows in trapezoidal silicon microchannels, Int. J. Heat Mass Transfer 43 (2000) 353–364.

[5] W. Qu, G.M. Mala, D. Li, Heat transfer for water flows in trapezoidal silicon microchannels, Int. J. Heat Mass Transfer 43 (2000) 3925–3936.

[6] A.G. Fedorov, R. Viskanta, Three-dimensional conjugate heat transfer in the microchannel heat sink for electronic packaging, Int. J. Heat Mass Transfer 43 (2000) 399–415.

[7] K. Kawano, K. Minakami, H. Iwasaki, M. Ishizuka, Development of microchannels heat exchanging, in: R.A. Nelson Jr., L.W. Swansin, M.V.A. Bianchi, C. Camci (Eds.), Application of Heat Transfer in Equipment, Systems, and Education, HTD-vol. 361-3/PID-vol. 3, ASME, New York, 1998, pp. 173–180.

[8] S.K. Lim, K.T. Ooi, T.N. Wong, K.C. Toh, K. Suzuki, Experimental investigation of liquid flow in a micro-tube, Engineering advances at the dawn of the 21st century, in: Proceedings of the Seminar on Integrated Engineering, 2000, pp. 487–493.

[9] S.K. Lim, T.N. Wong, K.T. Ooi, K.C. Toh, K. Suzuki, Analytical study of liquid flow in a micro-tube, Engineering advances at the dawn of the 21st century, in: Proceedings of the Seminar on Integrated Engineering, 2000, pp. 472–478.

[10] V.K. Samalam, Convective heat transfer in microchannels, J. Electron. Mater. 18 (1989) 611–617.

[11] D.B. Tuckerman, Heat transfer microstructures for integrated circuits, Ph.D. thesis, Stanford University, 1984.

[12] A. Weisberg, H.H. Bau, J.N. Zemel, Analysis of microchannels for integrated cooling, Int. J. Heat Mass Transfer 35 (1992) 2465–2474.

[13] E.Y.K. Ng, C.P. Tso, Z.M. Wen, K.F. Choo, Numerical simulation of flow and conjugate heat transfer in a microchannel for electronics cooling, J. Electron. Manuf. 9 (1999) 141–153.

[14] S.V. Patankar, Numerical Heat Transfer and Fluid Flow, Hemisphere, New York, 1980.

[15] F. Incorpera, Liquid Cooling of Electronic Devices by Single-Phase Convection, Wiley, 1999.